Toward optimization of stiffness and flexibility of rigid, flat-foldable origami structures

Evgueni T. Filipov, Tomohiro Tachi, and Glaucio H. Paulino

Abstract. Origami patterns have been applied in spatial structures to make stiff shell structures as well as flexible transformable systems. Folding a planar sheet into a 3D configuration changes the stiffness and the behavior of the sheet. In this paper we discuss a scalable analytical model for simulating origami structures, and we use eigenvalue band-gaps to optimize both the flexibility and stiffness of the system. We focus our study on rigid, flat foldable tubes and investigate the influence that different parameters have on the stiffness characteristics.

1. Introduction

Rigid foldable origami consists of stiff panel elements connected by flexible fold or hinge elements. The premise of these origami patterns is that they can fold and unfold without deforming the panel elements, which makes these systems especially useful for large-scale structural applications where thickened panels can be connected with more flexible hinge elements [**14, 15**]. In reality, rigid origami structures can experience deformations that do not correspond to rigid folding and thus the stiffness behavior of such systems is of great interest [**11, 17**]. Amongst various origami patterns, the Miura-ori folding pattern has gained substantial interest in the past years because it allows flat and rigid folding of a sheet [**7, 8, 11, 17, 3, 12**], and recently Miura like patterns have also been used to create tubular structures that are also flat and rigid foldable [**13, 16, 9**].

Furthermore, optimization for folding systems has also been a topic of interest in recent years. For example, Fuchi and Diaz [**2**] have shown an optimization algorithm that uses a ground structure approach to find a folding pattern with desired geometric properties and a minimum number of crease lines. Other research has optimized bistable compliant mechanisms to design retractable structures that require minimal force for deployment [**10**]. Optimization for the stiffness of origami structures, however, has not yet been explored in detail.

In this paper we discuss ideas for optimizing the stiffness of rigid foldable structures. Stiffness modeling is especially important in optimization problems [**4**]. In

---

This work was partially funded by the National Science Foundation (NSF) through grants CMMI 1234243 and CMMI 1321661. The first author is grateful for support from the NSF Graduate Research Fellowship, and the Japan Society for the Promotion of Science Fellowship. We also acknowledge support from the Donald B. and Elizabeth M. Willett endowment at the University of Illinois at Urbana-Champaign.

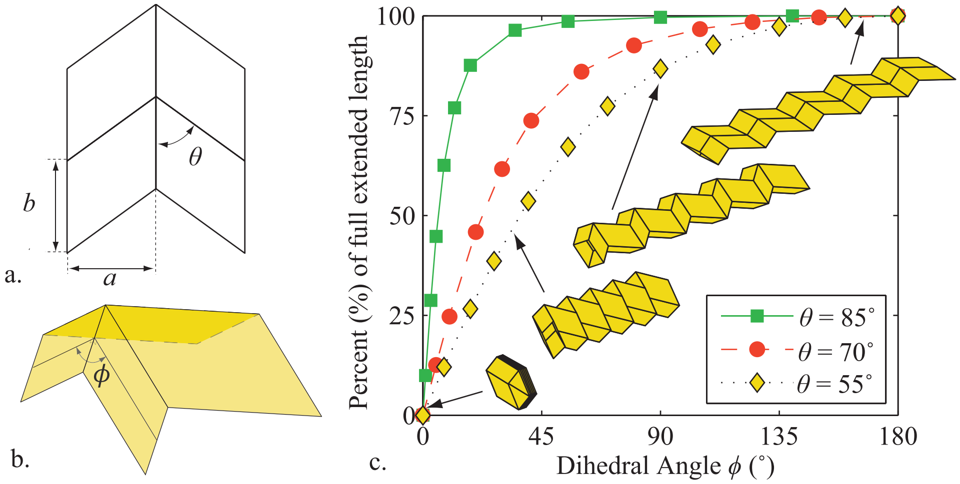

FIGURE 1. Construction of a rigid and flat foldable origami tube: (a) definition of a single Miura cell, (b) folding definition for the Miura cell, (c) dihedral angle ϕ vs. tube length as a percent(%) of the maximum extension length for tubes with $\theta = 55°$, $\theta = 70°$, and $\theta = 85°$. The tube with $\theta = 55°$ is shown folded at $\phi = 2°, 35°, 90°$, and $170°$

this paper we improve upon an established model [**11**], and create a scalable model that takes into account the elastic modulus and thickness properties of the flexible material. We explore methods for modeling the bending of prescribed origami folds, bending of the more stiff origami panels, and shear and tensile stretching of these panels. We study the global stiffness of the Miura inspired tube structures [**13**] by investigating the eigenvalues and corresponding eigen-modes of the stiffness matrix. The first six eigen-modes correspond to rigid body motion in 3 dimensional space, the next mode corresponds to the rigid folding motion, and subsequent modes represent structural deformation. We use constraints on the pattern to ensure that it remains flat and rigid foldable, and we then modify the geometry to show optimal cases for structural stiffness and flexibility. By varying geometric parameters we can minimize or maximize the seventh and/or subsequent eigenvalues of the structure. Minimizing an eigenvalue makes the structure more flexible, and easier to fold, whereas maximizing an eigenvalue makes the structure stiffer. Similarly, eigenvalue band-gap maximization can be used to simultaneously control two eigen-modes. This procedure can be used to minimize the rigid folding eigen-mode, making the structure easier to fold and deploy, while at the same time it would maximize the bending modes causing the structure to be stiffer for external loadings.

The paper is organized as follows: Section 2 discusses the geometric properties of the rigid flat foldable origami tubes studied in this paper; Section 3 presents numerical methods for simplified scalable modeling of origami systems; the general stiffness properties of the tubes is discussed in Section 4; Section 5 provides optimal cases for the origami tube structures; and Section 6 presents concluding remarks.

2. Rigid and flat foldable origami tubes

In this work we restrict our study to a simple subset of the origami tubes that is available in the literature. Fig. 1 shows the definition of a Miura cell in our study. The acute vertex angle θ along with the dimensions a and b are sufficient to define the Miura cell, and the dihedral angle ϕ can be used to define the folded configuration of the cell. The Miura cell is then repeated, and reflected to create a tube. For example, Fig. 1 (c) shows a tube that is 10 panels (5 cells) long and is folded in different configurations. The tube is flat foldable in both directions, and the total extended length of the tube L_{Ext} can be calculated as:

$$L_{EXT} = Na\frac{\tan(\theta)\sin(\phi/2)}{\sin(\theta)\sqrt{1+\tan(\theta)^2\sin(\phi/2)^2}} \tag{2.1}$$

where N is the number of panels repeating in the direction of a. The maximum (full) length (L_{Full}) that the tube can reach (when $\phi = 180°$) stays constant if the parameters a and N are fixed, and the total area of the panels will also remain constant if the parameters a and b are fixed. Fig. 1 (c) shows how different structures ($\theta = 85°; \theta = 70°;\text{and}\theta = 55°$) expand at different rates when related to the dihedral angle. Thus, it is also useful to consider the percentage of the the full extended length when comparing the configuration of different structures, as this quantity gives a physical definition of the deployment of the structure.

3. Modeling of origami structures

When performing structural optimization, it is especially important that the mechanics of the analytical models are properly defined. If not, it is common for the optimization procedure to find local minima that are artifacts of the numerical model. In this section we describe the numerical modeling of thin sheets in origami systems. A previously established model [**11**] is used as a basis, and several improvements are discussed. We incorporate scaling effects for the structure and make the panel stiffness dependent on the thickness (t), the elastic modulus (E), and Poisson's ration (ν) of the material. The formulation for fold modeling is also updated, and a ratio is used to relate the bending stiffness of panels to the bending stiffness of a fold. The model provides an improved basis for origami stiffness simulation, while keeping the formulation simple and modeling the origami components (panels and folds) as individual elements. The simplicity of this model makes it a good option for origami optimization, but we also acknowledge that it is not an ideal substitution to a detailed finite element (FE) model composed of nonlinear shell elements. The stiffness matrix ($\mathbf{K}$) for the origami structure incorporates stiffness parameters for 1) panels stretching and shearing ($\mathbf{K}_S$); 2) panels bending ($\mathbf{K}_S$); and 3) bending of prescribed fold lines ($\mathbf{K}_F$). The global stiffness matrix is constructed as follows:

$$\mathbf{K} = \begin{bmatrix} \mathbf{C} \\ \mathbf{J}_B \\ \mathbf{J}_F \end{bmatrix}^T \begin{bmatrix} \mathbf{K}_S & 0 & 0 \\ 0 & \mathbf{K}_B & 0 \\ 0 & 0 & \mathbf{K}_F \end{bmatrix} \begin{bmatrix} \mathbf{C} \\ \mathbf{J}_B \\ \mathbf{J}_F \end{bmatrix} \tag{3.1}$$

where the compatibility matrix ($\mathbf{C}$) and Jacobian matrices ($\mathbf{J}_B$ and $\mathbf{J}_F$) relate the stiffness of elements to the nodal displacements as discussed in detail in Sections 3.1 to 3.1. Each node has three degrees of freedom (x, y and z displacement), and the stiffness matrix is of size ($N_{dof} \times N_{dof}$), with N_{dof} representing the total number

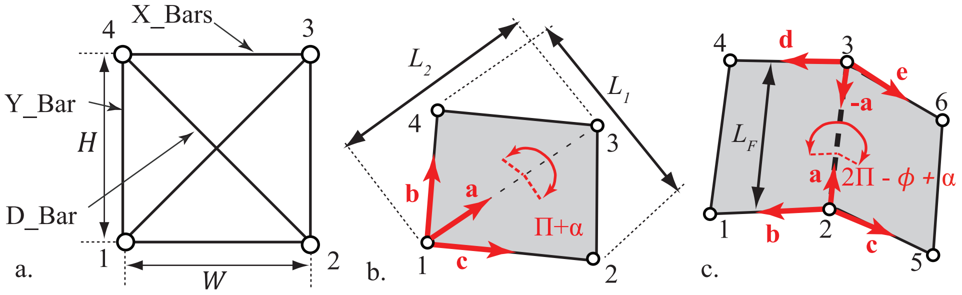

FIGURE 2. Model schematics for:(a) bars simulating panel stretching and shear, (b) rotational hinge for panel bending, (c) rotational hinge simulating bending along a prescribed fold line

of degrees of freedom in the system. The mass for each panel is calculated from the panel volume and the material density ρ. A mass matrix $\mathbf{M}$ for the entire structure is constructed by distributing 1/4 of the panel mass to each of the connecting nodes.

3.1. Panel stretching and shearing (Bar modeling). The stiffness of panels for in-plane, axial and shear loads is simulated using the indeterminate bar frame shown in Fig. 2 (a). A general formulation for bar elements is used with: an equilibrium matrix ($\mathbf{A}$) relating internal bar forces ($\mathbf{t}$) to nodal forces ($\mathbf{f}$) as $\mathbf{At} = \mathbf{f}$; a compatibility matrix($\mathbf{C}$) relating bar nodal displacements ($\mathbf{d}$) to bar extensions ($\mathbf{e}$) as $\mathbf{Cd} = \mathbf{e}$; and finally a diagonal matrix ($\mathbf{K}_S$) relating the bar extensions to the local forces as $\mathbf{K}_S\mathbf{e} = \mathbf{t}$. As further described in [**11**], using the static-kinematic duality that $\mathbf{C} = \mathbf{A}^T$, the linear system for stretching and shear of the panels (i.e. the bars) is represented as the first row of Equation 3.1. The crossed bar frame (Fig. 2 (a)) has six bars connected only at the four corner nodes of the origami panel. This crossed bar geometry was chosen since individual bar properties can be defined, such that the entire frame behaves as an isotropic panel. The bar stiffness parameters (i.e. components of $\mathbf{K}_S$) are defined for each bar as:

$$K_S = \frac{EA_B}{L_B} \tag{3.2}$$

where L_{Bar} is the bar length, and the bar area, A_B, is defined differently for the horizontal (X Bars), vertical (Y Bars), and diagonal bars (D Bars). Appendix A contains a detailed discussion on how the bar areas are defined to achieve isotropic material behavior for the entire panel. The model exhibits realistic tensile and shear stiffness behavior when a Poisson's ratio of $\nu = 1/4$ is used in the formulation.

3.2. Panel bending modeling. The stiffness of the panels in bending is simulated as an angular constrain between two adjacent facets of the panel. Fig. 2 (b) shows a model schematic of a panel bending along the diagonal 1-3. For small deformations the choice of the diagonal does not affect the kinematics, however it affects the stiffness formulation [**12**]. Similar to previous research we formulate our model assuming that bending occurs along the shorter diagonal, since the bending energy will be lower along the shorter path. An angular constraint F is formulated based on the dihedral bending angle α. As shown in [**11**], the angle can be calculated by using cross and inner products of the vectors **a**, **b**, and **c** that are based on the nodal coordinates of the panel **p**. The constraint can be defined as:

$$F = \sin(\alpha(\mathbf{p})) \tag{3.3}$$

and a corresponding Jacobian for the panel bending $\mathbf{J}_B$ is calculated as:

$$d\alpha = \frac{1}{\cos(\alpha)} \sum \frac{\partial F}{\partial p_i} dp_i = \mathbf{J}_B \mathbf{d} \tag{3.4}$$

where **d** are the displacements of the panel nodes. The second row of Equation 3.1 incorporates the panel bending by using the Jacobian matrix with the diagonal matrix $\mathbf{K}_B$ to incorporate the stiffness corresponding to each panel.

Assuming the in-plane stiffness of the paper is high enough to prevent local buckling, then the panel is expected to bend with curvature only in one direction, as discussed in [**1**]. This phenomena is especially similar to the bending of thin sheets with restrained edges that has been studied in some detail over the past years [**6, 5, 18**]. The bending energy of thin sheets with restrained edges is somewhat higher, since tensile forces develop over the sheet's surface, and flexural deformations become restricted to a small length, that is focused near the bending ridge (i.e. the diagonal 1-3 in Fig. 2 (b)). Due to this phenomena, the elastic energy of the panel bending scales approximately as $k(L_2/t)^{1/3}$ where k is the bending modulus of the sheet, defined as $k = \frac{Et^3}{12(1-\nu^2)}$ [**5**]. We choose to calculate the individual panel stiffness as:

$$K_B = C_B \frac{Et^3}{12(1-\nu^2)} \left(\frac{L_2}{t}\right)^{1/3} \tag{3.5}$$

since this incorporates the effect of the L_2/t ratio in restricting the bending of a thin sheet. The factor C_B is set to 0.794 based on approximations from numerical results in [**5**]. This methodology has not been validated for origami systems so the authors believe that future experimental studies can better verify the scaling properties of thin panels in origami and can substantiate the constant C_B. The definition in Equation 3.5, tends to be stiffer than if we were to assume constant curvature bending of the sheet.

3.3. Fold bending modeling.

Modeling of the fold component of the origami structure is in many ways similar to the model for bending of panels. Realistic origami behavior does not allow for significant out of plane deformations along fold lines as discussed by [**1**], and thus it is sufficient to use a simplified approach to model the origami fold as a rotational spring along a line. Fig. 2 (c) shows the model for a fold spanning between nodes 2 and 3 that connects two panels (1-2-3-4 and 2-5-6-3). The length of the fold is L_F and the stiffness is expected to scale linearly with this length since curvature and bending energy are expected to exist only on the infinitesimally small width of the fold. The same constraint formulation presented in 3.2 is used to formulate two independent fold elements from the two vector sets: (1) **a**, **b**, and **c** and (2) **-a**, **d**, and **e**. This approach distributes the stiffness of the fold to all relevant nodes on the two adjacent panel elements.

The actual behavior and stiffness of origami folds is not well understood yet. For now we assume only elastic deformations occur, and we assume that the folds are less stiff then the bending of panels. A factor R_{FP} is introduced to relate the stiffness between the bending of a fold with length $L_F = 1$ and the bending of a panel with a diagonal of $L_2 = 1$. For our analyses we use $R_{FP} = 1/10$, however

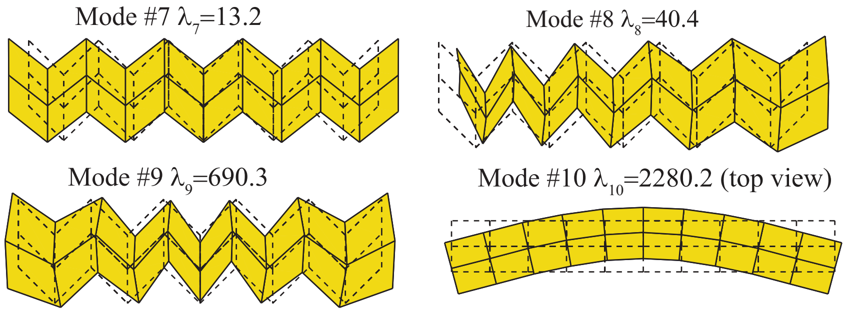
Mode #7 λ_7=13.2

Mode #8 λ_8=40.4

Mode #9 λ_9=690.3

Mode #10 λ_{10}=2280.2 (top view)

Figure 3. Normalized mode shapes #7 to #10 of tube structure with $\theta = 55°$ and $a = b = 1$ when it is deployed to $\phi = 90°$. Note: the undeformed configurations of the tube are shown as dotted lines.

the value of this quantity should be further investigated. For the fold stiffness, we obtain an equation similar to (3.5), that scales linearly with L_F:

$$K_F = R_{FP} \frac{L_F}{2} C_B \frac{Et^3}{12(1-\nu^2)} \left(\frac{1}{t}\right)^{1/3} \tag{3.6}$$

4. Stiffness properties of tube structures

Eigenvalue analyses are used to study the stiffness and flexibility of the origami structures. The linear dynamics system is used to solve the underlying eigenvalue problem formulated as:

$$\mathbf{K} v_i = \lambda_i \mathbf{M} v_i, \;\; i = 1, ..., N_{dof} \tag{4.1}$$

where λ_i is the i^{th} eigenvalue and v_i is the corresponding eigen-mode of the structure. A base case of the analysis is shown in Fig. 3 for a tube where $\theta = 55°$ and $N = 10$, and $a = b = 1$. The thickness of the material is $t = 0.01$, the Young's modulus is $E = 10^6$, the Poisson's ratio is $\nu = 1/4$, the density is $\rho = 1$, and the factor relating fold to panel stiffness is $R_{FP} = 1/10$. The first six eigen-modes correspond to rigid body motion of the structure in 3 dimensional space so they are omitted in our study. Fig. 3 shows the eigen modes corresponding to the 7th to 10th eigenvalues of the structure when deployed to a configuration with $\phi = 90°$. The rigid folding motion corresponds to the 7th mode of the structure where the system can fold and unfold without deforming the panel elements, and thus deformation occurs primarily in the more flexible fold elements. The 8th mode is a type of "squeezing" mode, where one end of the structure is folded while the other end is unfolded. This mode results in bending of the fold and the panel elements, however, the panels do not stretch or shear, and thus the total energy is only slightly higher than that of the 7th eigen-mode. Subsequent modes contain stretching and shearing of the panels which requires much higher energy than the bending deformations.

Fig. 4 (a) shows the behavior of the eigenvalues for the structure in Fig. 3 compared to the dihedral angle ϕ. There is substantial mode switching for higher modes and at the extreme ends of the spectrum. The mode switching is a result of the changing geometry of the structure, for example, when the structure reaches a nearly flattened state $\phi \approx 180°$, bending of the structure globally (mode #10 at

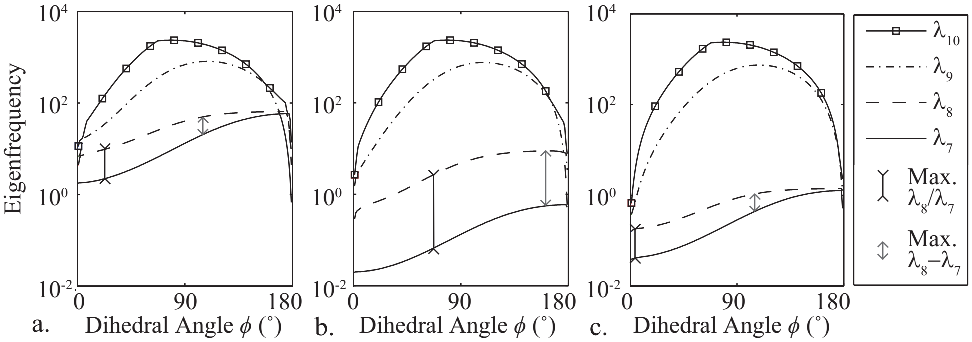

FIGURE 4. (a) Eigenvalue spectrum for the base tube structure ($\theta = 55°$, $a = b = 1$, $N = 10$, $t = 0.01$, $E = 10^6$, $\nu = 1/4$, $\rho = 1$, and $R_{FP} = 1/10$) through the deployment ($\phi = 0° - 180°$), (b) eigenvalue spectrum for the structure now with $R_{FP} = 1/1000$, (c) eigenvalue spectrum for the structure now with $t = 0.001$.

$\phi = 90°$) becomes easier than folding of the structure. Fig. 4 (b) shows the effect of reducing the factor R_{FP}, when keeping all other parameters of the analysis the same. The fold elements become, much more flexible, and the 7th and 8th eigenvalues drop. Since the 7th mode depends only on the fold elements, its eigenvalue drops more substantially and the gap λ_7 and λ_8 is effectively enlarged. In practice this type of behavior can be achieved through making the panels out of thick rigid material, while making the folds from thinner and more flexible material e.g. cloth. In Fig. 4 (c) we show the behavior of the structure with the thickness reduced to $t = 0.001$, but all parameter are kept the same as before. Reducing the thickness of the material reduces the axial and shear stiffness linearly, but the bending stiffness of the panels and folds is reduced at a much higher rate ($t^{2\frac{2}{3}}$). Due to this both the 7th and 8th eigenvalues drop substantially. Note that since the mass and axial/shear stiffness both vary linearly with the thickness, modes 9 and higher are not substantially influenced by this change.

5. Optimization for tube structures

For practical applications, architects and engineers may want to improve the stiffness characteristics of origami structures by minimizing or maximizing certain eigenvalues of the structure. Minimizing an eigenvalue would make the structure more flexible in the corresponding mode and maximizing it would make the structure stiffer. For example, it would be beneficial to minimize the 7th eigenvalue thus making the structure easier to deploy, but it would also be beneficial to increase the 8th and subsequent modes to make the structure stiffer for other loading scenarios. This can be achieved by performing optimization to maximize the ratio λ_8/λ_7 or the gap $(\lambda_8 - \lambda_7)$. The ratio λ_8/λ_7 is a good theoretical benchmark where the 8th eigenvalue is the highest in relation to the 7th, while the gap $(\lambda_8 - \lambda_7)$ is a more practical solution where there is the largest physical space between the two eigenvalues. In this study we choose to focus on the gap $(\lambda_8 - \lambda_7)$, but using the ratio could also be used to provide interesting results. To gain a better understanding of

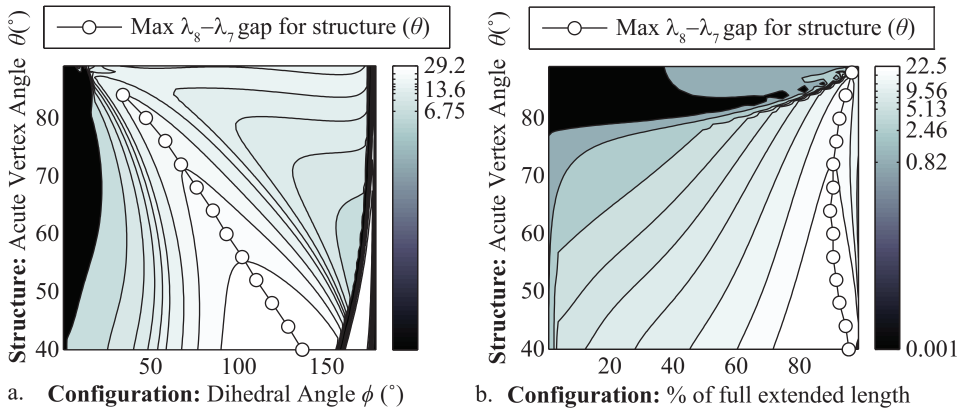

FIGURE 5. Structure definitions and configurations that maximize the gap $(\lambda_8 - \lambda_7)$ for tube with $a = b = 1$ and $N = 10$ (a) Dihedral angle (ϕ) vs. Acute vertex angle (θ), (b) Percent (%) of full extended length vs. Acute vertex angle (θ). Note: logarithmic scale used

the tube stiffness and the influence of the geometric parameters, we perform several optimization cases by using only one variable to modify the structure geometry and one variable to define the configuration. For all of our optimization examples a generalized objective function and constraints are:

$$\begin{aligned} &\max_{(\theta,t,a,b,N,\phi)} \beta = (\lambda_8 - \lambda_7) \\ &\text{s.t. } L_{Full}(a,N) = aN = L_s \\ &\qquad V(a,b,t,N) = 4abtN = V_s \end{aligned} \tag{5.1}$$

where β is the band-gap, L_{Full} is the full extension length, and V is the volume of a given tube. These quantities are constrained to be the same as those of the analysis in Section 4, so $V_s = 0.40$ and $L_s = 10$.

5.1. Optimization with respect to the acute vertex angle θ. The first optimization case uses the acute vertex angle θ as the design variable to define the structure, and since this has no effect on the length or volume, all other quantities defining the structure are kept the same. Fig. 5 (a) shows the gap $(\lambda_8 - \lambda_7)$ with respect to the dihedral angle ϕ and θ. In the early and late phases of the deployment ($\phi < 10°$ and $160° < \phi$) there are locations of local minima and maxima, and these can be attributed to the mode switching that occurs in those regions. In the medium range of deployment, there is a smoother variation in magnitude of the gap $(\lambda_8 - \lambda_7)$ and lines show the configuration at which the maximum gap can be obtained for each structure (θ). Structures with high θ perform better (have a higher gap) when ϕ is lower, and the optimal dihedral angle grows as θ decreases. However, Fig. 5 (a) is somewhat misleading since for each structure, the angle ϕ corresponds to a different configuration in the expansion sequence as shown in Fig. 1 (c).
Alternatively, Fig. 5 (b) shows the gap instead defining the configuration as a percentage (%) of the full extended length (L_{Full}). When using this measure, it is apparent that the structures (regardless of θ) reach their optimal point at about 95%

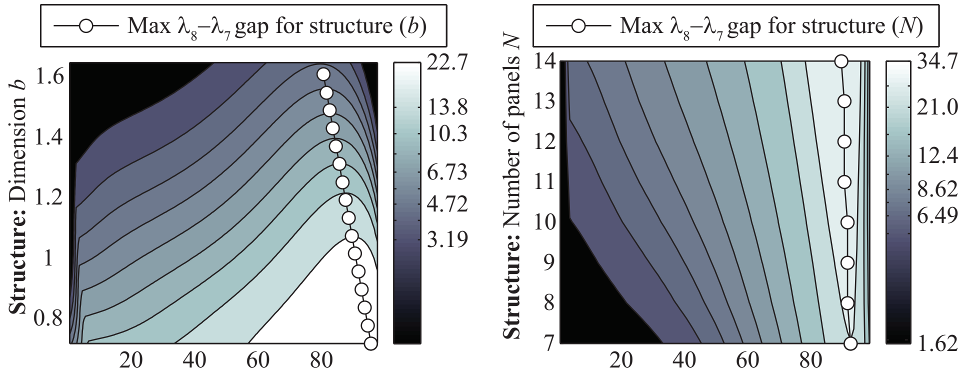

a. **Configuration:** % of full extended length b. **Configuration:** % of full extended length

Figure 6. Structure definitions and configurations that maximize the gap ($\lambda_8 - \lambda_7$) for structure where $\theta = 55°$ (a) and $N = 10$: Percent (%) of full extended length vs.dimension b, (b) and $a = 10/N$: Percent (%) of full extended length vs. Number of panels (N)

expansion. The gap for structures with $\theta > 80°$ is especially low in early phases of the deployment, since in those phases, these tubes are susceptible to bending modes and mode switching. Furthermore, tubes with lower θ have a higher gap for all configurations with respect to the expansion. This is because panel bending in mode #8 becomes more pronounced for lower θ, and thus λ_8, and gap become higher. In other words, mode #8 occurs with little panel bending when θ is high, and thus the energy and λ_8 are lower.

5.2. Optimization with respect to panel dimension b. For Fig. 6 (a) the base structure ($\theta = 55°$)is used again and dimension b is used as the design variable to study its effect on the gap ($\lambda_8 - \lambda_7$). The number of panels and variable a are kept the same, and thus the thickness of the panels is defined as $t = 0.01/b$ to maintain a constant volume for the structure. The results for this analysis, when using the expansion length to define the configuration are shown in Fig. 6 (a). Again, all structures reach their optimal point when in a configuration that is close to fully extended (80%-97%). Furthermore, structures where the dimension b is lower and the thickness t is higher have a higher gap ($\lambda_8 - \lambda_7$). This phenomena can be attributed to two factors: 1) the panel and fold stiffness with $t^{2\frac{2}{3}}$ as t increases and λ_8 increases more since it engages both fold and panel elements, and 2) smaller panels are stiffer than larger panels, note that the rotational hinge stiffness (defined through J_P) varies with respect to L_1^2.

5.3. Optimization with respect to the number of panels N. A final optimization case uses the number of panels (N) as the design variable, a is re-defined as $a = 10/N$ to satisfy the constraints V_s and L_s, and all other tube parameters are kept the same. Fig. 6 (b) shows the results for this analysis. The structures with more panels tend to have only a slightly higher band gap than structures with the same parameters, but less panels. With more panels the length L_2 is reduced and the energy of each panel in bending decreases as $L_2^{1/3}$, however since more panels are added the total energy in for mode #8 and λ_8 increase slightly.

6. Conclusions

This paper first describes a computational method for modeling the stiffness characteristics of origami structures. We introduce simplified scalable measures for the stretching, shear and bending of thin elastic sheets, as well as the stiffness of more flexible prescribed fold lines. The computational method is used to perform elastic eigenvalue analyses to study the behavior of rigid, flat, foldable tube structures that are derived from the Miura-ori pattern. The energies of different eigen-modes are studied, and optimization is performed to maximize the band-gap between the 7^{th} and 8^{th} modes, as this makes the structure more flexible for deployment, yet stiffer for other loading cases. To increase the band gap, a trivial solution would be to make the folds out of much more flexible material than the panels, thus making the rigid folding mode very soft. Alternatively, designers may choose to: 1) use structures with lower acute vertex angle θ, 2) use a smaller tube height b and instead make the material proportionally thicker, or 3) use more panels over the length of the structure. The analysis techniques and optimization methods described in this paper are intended to enable researchers to optimize stiffness in origami systems.

Appendix A. Bar element definitions

The indeterminate bar frame shown in Fig. 2 (a) can be defined such that it will exactly exhibit Poisson effects for tensile loading in both directions (i.e. isotropic behavior). This can be achieved when the bar areas of Equation 3.2 are defined as:

$$A_{X\_Bars} = t\frac{H^2 - \nu W^2}{2H(1-\nu^2)} \tag{A.1}$$

$$A_{Y\_Bars} = t\frac{W^2 - \nu H^2}{2W(1-\nu^2)} \tag{A.2}$$

$$A_{D\_Bars} = t\frac{\nu(H^2 + W^2)^{3/2}}{2HW(1-\nu^2)} \tag{A.3}$$

for the horizontal (X Bars), vertical (Y Bars), and diagonal bars (D Bars) respectively. The variable H is the height, and W the width of the panel. Fig. 7 (a) shows the frame model defined with $W = H = 1$, $t = 0.01$, $E = 1000$, $\nu = 1/3$ and subjected to a tensile patch test. Fig. 7 (b) shows the same frame model subjected to a shear patch test. In shear loading, the model behavior is highly dependent on the chosen Poisson's ratio. As can be observed from Equation A.3, when a low ν is used, the diagonal bars have a low area and this results in the frame having a low shear stiffness. The converse is also true, and this relation is opposite to the realistic shear behavior of isotropic materials. However, when ν is set to $1/3$ the frame model behaves exactly the same in shear as a homogeneous, isotropic block of material. The diagonal bars each carry a force of $F/2$ in the x direction, and a lateral displacement occurs based on the bar stiffness definition (i.e. Equations 3.2 and A.3). When $\nu = 1/3$ the bar frame displacement exactly matches the lateral displacement of a solid block with dimensions $W \times H \times t$ loaded in pure shear, analytically defined as:

$$\Delta_x = \frac{FH}{GWt} \tag{A.4}$$

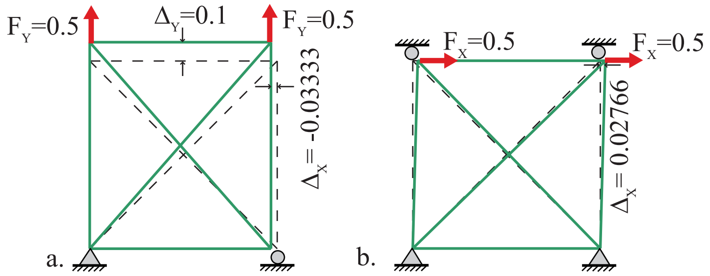

Figure 7. Bar model for simulating panel stretching and shear: (a) tensile patch test of model (original configuration shown with dashed line) (b) shear patch test of model

where F is the total shear force, and G is the shear modulus that can be defined as $G = \frac{E}{2(1+\nu)}$ for a homogeneous, isotropic, linear elastic material. With $\nu = 1/3$, the frame is scale independent for shear loadings, and furthermore if the problem in Fig. 7 (c) is re-meshed, then the frame model converges to the same solution as any generic FE approach. However, since only a single six-bar frame is used to model each panel, the shear stiffness of the panel is over-estimated by this model (similarly to FE approaches). In reality, the shear patch test converges to higher displacement than the exact solution from Equation A.4, since in addition to the shear deformations, tensile deformations also occur over the width and height of the patch. Using a lower Poisson's ratio we can artificially reduce the shear stiffness of the frame, so we choose to instead use $\nu = 1/4$, since at this ratio a single bar frame exhibits approximately the same shear deformation the patch test performed on a mesh of 2500 finite elements.

References

1. Erik D. Demaine, Martin L. Demaine, Vi Hart, Gregory N. Price, and Tomohiro Tachi, *(Non)existence of pleated folds: How paper folds between creases*, Graphs and Combinatorics **27** (2011), no. 3, 377–397.
2. Kazuko Fuchi and Alejandro R. Diaz, *Origami design by topology optimization*, Journal of Mechanical Design **135** (2013), no. 11, 111003.
3. Joseph M. Gattas, Weina Wu, and Zhong You, *Miura-base rigid origami: parameterizations of first-level derivative and piecewise geometries*, Journal of Mechanical Design **135** (2013), no. 11, 111011.
4. Raphael T. Haftka and Zafer Gürdal, *Elements of Structural Optimization*, Springer Science & Business Media, 1992.
5. Alexander Lobkovsky, *Boundary layer analysis of the ridge singularity in a thin plate*, Physical Review E **53** (1996), no. 4, 3750–3759.
6. Alexander Lobkovsky, Sharon Gentges, Hao Li, David Morse, and Thomas A. Witten, *Scaling properties of stretching ridges in a crumpled elastic sheet*, Science **270** (1995), no. 5241, 1482–1485.
7. Lakshminarayanan Mahadevan and Sergio Rica, *Self-organized origami.*, Science (New York, N.Y.) **307** (2005), no. 5716, 1740.
8. Koryo Miura, *The science of Miura-ori: A review*, Origami 4 (Robert J. Lang, ed.), AK Peters, 2009, pp. 87–99.
9. Koryo Miura and Tomohiro Tachi, *Synthesis of rigid-foldable cylindrical polyhedra*, Journal of the International Society for the Interdisciplinary Study of Symmetry (2010), 204–213.
10. Makoto Ohsaki, Seita Tsuda, and Hidekazu Watanabe, *Optimization of retractable structures utilizing bistable compliant mechanism*, Engineering Structures **56** (2013), 910–918.

11. Mark Schenk and Simon D. Guest, *Origami folding: A structural engineering approach*, Origami 5: Fifth International Meeting of Origami Science, Mathematics, and Education (Patsy Wang-Iverson, Robert J. Lang, and Mark Yim, eds.), vol. 2, CRC, 2011, pp. 293–305.
12. ———, *Geometry of Miura-folded metamaterials.*, Proceedings of the National Academy of Sciences of the United States of America **110** (2013), no. 9, 3276–81.
13. Tomohiro Tachi, *One-dof cylindrical deployable structures with rigid quadrilateral panels*, Proceedings of the IASS Symposium, Editorial Universitat Politècnica de València, February 2009, pp. 2295–2305 (eng).
14. ———, *Simulation of rigid origami*, Origami4 (Robert J. Lang, ed.), AK Peters, 2009, pp. 175–187.
15. ———, *Rigid-foldable thick origami*, Origami 5: Fifth International Meeting of Origami Science, Mathematics, and Education (Patsy Wang-Iverson, Robert J. Lang, and Mark Yim, eds.), CRC, 2011, pp. 253–264.
16. Tomohiro Tachi and Koryo Miura, *Rigid-foldable cylinders and cells*, Journal of the International Association for Shell and Spatial Structures **53** (2012), no. 4, 217–226.
17. Zhiyan Y. Wei, Zengcai V. Guo, Levi Dudte, Haiyi Y. Liang, and Lakshminarayanan Mahadevan, *Geometric mechanics of periodic pleated origami*, Physical Review Letters **110** (2013), no. 21, 215501.
18. Thomas Witten, *Stress focusing in elastic sheets*, Reviews of Modern Physics **79** (2007), no. 2, 643–675.

University of Illinois at Urbana-Champaign, Urbana, IL, USA
E-mail address: `filipov1@illinois.edu`

University of Tokyo, Tokyo, Japan
E-mail address: `tachi@idea.c.u-tokyo.ac.jp`

University of Illinois at Urbana-Champaign, Urbana, IL, USA
E-mail address: `paulino@illinois.edu`